

Radiative μ^- Capture in Copper*

WILLIAM T. CHU,[†] IRVING NADELHAFT, AND JULIUS ASHKIN
Carnegie Institute of Technology, Pittsburgh, Pennsylvania

The radiative capture of negative muons in copper ($\mu^- + \text{Cu} \rightarrow \text{Ni} + \nu + \gamma$) has been measured. The muons were captured in the copper plates of one spark chamber and the gamma rays converted in the lead plates of a second spark chamber. A large (8-in. \times 8-in.) NaI crystal was used to measure the gamma-ray energy. The apparatus was sensitive to gamma rays of energy larger than 50 MeV. The observed gamma-ray spectrum is compared to a theoretical spectrum based on a Fermi-gas model of the nucleus. This results in values for the branching ratio for radiative muon capture relative to ordinary muon capture of $R = (4.6 \pm 0.7) \times 10^{-4}$ for $M^* = M_p$ and $R = (5.2 \pm 0.8) \times 10^{-4}$ for $M^* = M_p/2$; where M^* is the effective nucleon mass used in the model, and M_p is the mass of the proton. An attempt is made to extrapolate the observations in copper to what might be expected for the case of a free proton.

I. INTRODUCTION

PRESENT experimental evidence on muon capture in the light nuclei (hydrogen¹ and helium^{3,2}), and on the branching ratio of pion decay $\pi \rightarrow e + \nu$ to $\pi \rightarrow \mu + \nu$, make it reasonable to accept as a working hypothesis the "universal Fermi interaction" (UFI), in which it is assumed that the role of the electron in β -decay coupling is identical to the role of the muon in the μ -capture coupling.

In addition to the large contributions of the axial vector A and vector V couplings, this model predicts smaller terms in the fundamental matrix element due to virtual strong interaction effects. Of particular importance is the exchange of a single pion between the baryons (p, n) and the leptons (μ, ν), as in Fig. 1, which produces an induced pseudoscalar coupling, g_P , proportional to the lepton mass, and hence more important for μ capture than for β decay. Theoretical estimates of the effective coupling constant $g_P^{(\mu)}$ have been made on this basis by Wolfenstein³ and by Goldberger and Treiman⁴ with the result that $g_P^{(\mu)}/g_A^{(\beta)} \approx 8$, where $g_A^{(\beta)}$ is the axial vector coupling constant in β decay. Exchange of additional pions and possibly other strongly interacting combinations will in general lead to further modification of the basic form factors for the interaction.

It must be recognized that ultimately a detailed knowledge of the μ -capture coupling can only come from more refined experiments on capture in the lightest nuclei. Such experiments, however, will require muon intensities far in excess of what is now available at synchrocyclotrons. It therefore appears reasonable at present to examine captures in heavier nuclei where specific effects may reveal special features of the capture interaction. The experiment reported here on the radiative muon capture process

$$\mu^- + (Z, A) \rightarrow (Z-1, A) + \nu + \gamma \quad (1)$$

for copper (natural isotopic abundance) has been undertaken in particular with the hope of obtaining evidence for the induced pseudoscalar interaction. The first observation of radiative capture (in iron) was made by Conversi⁵ and his collaborators at CERN using a spark chamber technique similar to the one used here. The same group⁶ has recently reported an experiment in calcium-40 using a counter technique with much-improved efficiency.

Theoretical discussions of the radiative capture process by a proton,⁷⁻¹¹

$$\mu^- + p \rightarrow n + \nu + \gamma, \quad (2)$$

have shown that the branching ratio of this process relative to nonradiative capture is very sensitive to the value of $g_P^{(\mu)}$. In Fig. 2, four of many possible Feynman diagrams for the radiative capture are shown. Figure 2(a) involves only the muon current and gives the principal contribution in a pure $V-A$ theory. Inclusion

* Supported in part by the United States Atomic Energy Commission.

[†] A thesis, based upon the work reported here (William T. Chu, NYO Report 10562, Carnegie Institute of Technology, January 1963) has been submitted to the Department of Physics, Carnegie Institute of Technology, in partial fulfillment of the requirements for the degree of Doctor of Philosophy. Author's present address: Brookhaven National Laboratory, Upton, Long Island, New York.

¹ R. H. Hildebrand and J. H. Doede, in *Proceedings of the 1962 Annual International Conference on High Energy Physics at Geneva* edited by J. Prentki (CERN, Geneva, 1962), p. 418; E. Bertolini, A. Citron, G. Gialanella, S. Focardi *et al.*, *ibid.*, p. 421; J. E. Rothberg, E. W. Anderson, E. J. Blesser, L. M. Lederman *et al.*, *Phys. Rev.* **132**, 2664 (1963).

² I. V. Falomkin, A. I. Filippov, M. M. Kulyukin, B. Pontecorvo *et al.*, *Phys. Letters* **3**, 229 (1963); L. B. Auerbach, R. J. Esterling, R. E. Hill, D. A. Jenkins *et al.*, *Phys. Rev. Letters* **11**, 23 (1963); R. M. Edelstein, D. Clay, J. W. Keuffel, and R. J. Wagner, Jr., Brookhaven National Laboratory Report BNL 837, 1963, p. 303 (unpublished).

³ L. Wolfenstein, *Nuovo Cimento* **8**, 138 (1958).

⁴ M. L. Goldberger and S. B. Treiman, *Phys. Rev.* **111**, 354 (1958).

⁵ G. Conforto, M. Conversi, and L. di Lella, *Phys. Rev. Letters* **9**, 22 (1962).

⁶ M. Conversi, R. Diebold, and L. di Lella, Brookhaven National Laboratory Report BNL 837, 1963, p. 315 (unpublished).

⁷ G. K. Manacher, thesis, Carnegie Institute of Technology, 1961, NYO Report 9284 (unpublished).

⁸ L. Wolfenstein, in *Proceedings of the 1960 Annual International Conference on High Energy Physics at Rochester*, edited by E. C. G. Sudarshan, J. H. Tinlot, and A. C. Melissinos (Rochester, New York, 1960), p. 529.

⁹ K. Huang, C. N. Yang, and T. D. Lee, *Phys. Rev.* **108**, 1340 (1957).

¹⁰ J. Bernstein, *Phys. Rev.* **115**, 694 (1959).

¹¹ G. A. Lobov and I. S. Shapiro, *Zh. Eksperim. i Teor. Fiz.* **43**, 1821 (1962) [English transl.: *Soviet Phys.—JETP* **16**, 1286 (1963)].

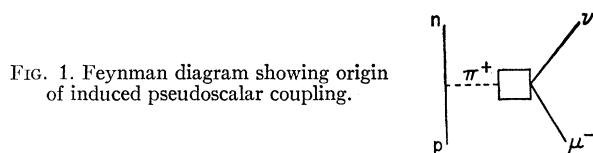


FIG. 1. Feynman diagram showing origin of induced pseudoscalar coupling.

of the diagrams of Figs. 2(b), (c), and (d) showing the induced pseudoscalar contribution gives an approximate doubling of the radiative capture branching ratio if $x \approx 8$. This enhancement arises to a large extent from the diagram Fig. 2(c) where radiation of a photon with energy comparable to the muon rest energy gives an especially large value for the single-pion propagator.

For radiative capture in a complex nucleus the desired information on the coupling constants must be obtained from the data only after first unfolding the complications due to effects of nuclear structure. The great sensitivity to the pseudoscalar coupling in (2), however, leads one to expect that in the *ratio* of radiative to ordinary capture, the sensitivity to $g_P^{(\mu)}$ will remain also in (1). To take a naïve and optimistic point of view one may hope that the branching ratio of the radiative capture in a complex nucleus is similar to that for capture by an ensemble of Z unpolarized protons, except that the ratio is reduced by a factor due essentially to a loss in phase space. Some support for this view comes from discussion of the complex nucleus case by Primakoff¹² and Cantwell¹³ using the $V-A$ theory, and from a recent discussion of Rood and Tolhoek¹⁴ on capture by calcium-40. We shall discuss our result on the radiative capture in copper using a related method. Nevertheless, it is our impression that the *numerical* estimates of $g_P^{(\mu)}$ based on these methods of reducing the experimental data have principally a qualitative significance.

The effect of an induced pseudoscalar coupling on the *total* capture rate of muons in complex elements is estimated to be about 20%.⁸ However, some partial rates have been shown¹⁵ to be quite sensitive to the value of $g_P^{(\mu)}$ and experiments taking advantage of this have been performed by groups at Columbia¹⁶ and Berkeley.¹⁷ Additional information bearing on $g_P^{(\mu)}$ comes from experiments which measure the neutron angular distribution when polarized muons are captured in spin-zero nuclei.^{18,19}

¹² H. Primakoff, Rev. Mod. Phys. **31**, 802 (1959).

¹³ R. M. Cantwell, Ph.D. thesis, Washington University, 1956 (unpublished).

¹⁴ H. P. C. Rood and H. A. Tolhoek, Phys. Letters **6**, 121 (1963).

¹⁵ I. S. Shapiro and L. D. Blokhintsev, Zh. Eksperim. i Teor. Fiz. **39**, 1112 (1960) [English transl.: Soviet Phys.—JETP **12**, 775 (1961)].

¹⁶ R. C. Cohen, S. Devons, and A. D. Kunaris, Phys. Rev. Letters **11**, 134 (1963).

¹⁷ A. Astbury, L. Auerbach, D. Cutts, R. Esterling, D. Jenkins *et al.*, Bull. Am. Phys. Soc. **9**, 81 (1964).

¹⁸ M. K. Akimova, L. D. Blokhintsev, and E. I. Dolinsky, Zh. Eksperim. i Teor. Fiz. **39**, 1806 (1960) [English transl.: Soviet Phys.—JETP **12**, 1260 (1961)].

¹⁹ V. S. Evseev, V. S. Roganov, V. A. Chernogorova, Chang Run-Hwa, and M. Szymczak, Phys. Letters **6**, 332 (1963).

II. EXPERIMENTAL METHOD

A. General

Since radiative capture is expected to occur with a branching ratio of about $\alpha/12\pi (=1.94 \times 10^{-4})$ relative to ordinary muon capture, it will form a rather small fraction of the total number of events in which negative muons disappear. Background problems are, therefore, likely to be serious. In particular, the observation of radiative capture is made difficult by the fact that the electrons from muons which decay can produce background gamma rays through external bremsstrahlung in the surrounding material. Since the upper limit of the gamma rays from radiative capture is of the order of 100 MeV, whereas the decay electron spectrum ends at about 53 MeV, it is possible to overcome this source of background by detecting only the upper end of the spectrum. In order to obtain information on the radiative capture spectrum below 50 MeV, one can try to subtract the contribution of the external bremsstrahlung by observing radiation from positive muons which are not captured and can therefore yield only external radiation. It is also essential to reduce the accidental background and to do this, a beam stretching technique was employed (described below).

In this experiment, the muon stopper and the gamma-ray converter were incorporated into spark chambers which were triggered by a delayed coincidence between a stopping muon and a subsequent gamma ray. This made it possible to select, on a visual basis, those events in which the spark chamber track of the μ stop and the tracks of the converted pair could be causally connected. Information on the time delay between the μ stop and the gamma ray was obtained by displaying counter pulses on the trace of a fast oscilloscope. The pulse height in a large NaI crystal was also displayed on the oscilloscope and gave information on the energy of the gamma ray.

B. Apparatus

A schematic diagram of the experimental apparatus is shown in Fig. 3. A beam of 70-MeV negative muons produced by the Carnegie Institute of Technology synchrocyclotron was brought to rest inside one of five copper plates of the Cu spark chamber (SC1). Counters 1, 2, and 3 in coincidence, and counter 4 and the water

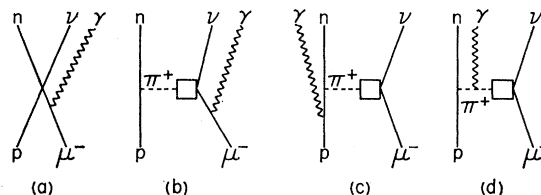


FIG. 2. (a) One of the Feynman diagrams for radiative capture. Contribution of the induced pseudoscalar is omitted. (b), (c), and (d) are typical diagrams in which the effect of the induced pseudoscalar is included.

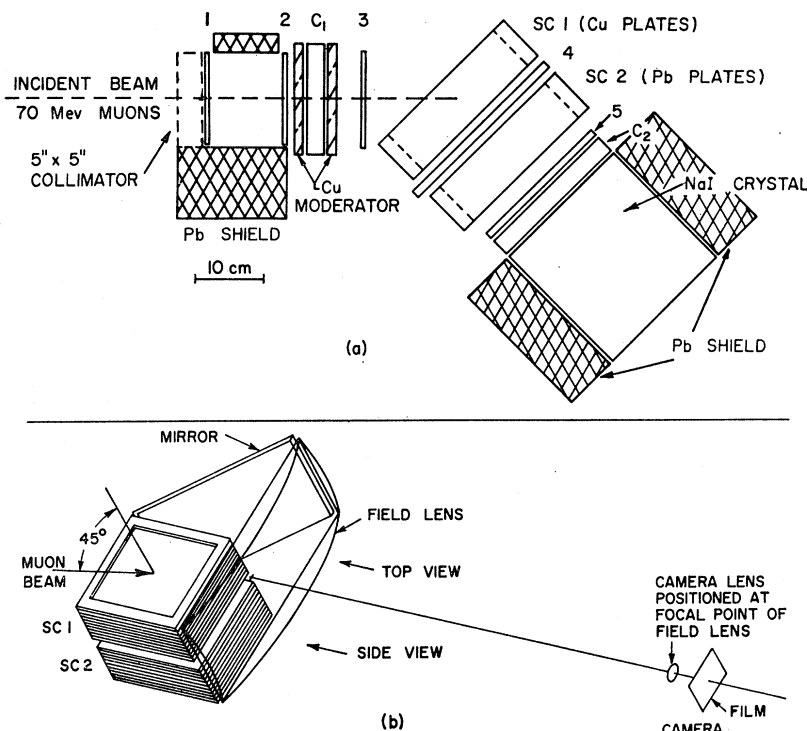


FIG. 3. (a) Side elevation of apparatus. (b) Detail showing spark chamber photography. The field lens focal length was 84 in.

Čerenkov counter (C_1) in anticoincidence, i.e., $1234\bar{C}_1$, defined the μ stop. The Čerenkov counter C_1 was used to discriminate against electrons in the beam. Gamma rays were detected by a coincidence of counters 5, C_2 , and a large NaI crystal, in anticoincidence with counters 1 and 4. Counter C_2 was a Lucite Čerenkov counter used to discriminate against charged particles other than electrons in the gamma-ray telescope. Counter 1 was placed in anticoincidence to eliminate events in which the gamma ray was in prompt coincidence with a particle in the incident beam. The gamma-ray signature was thus " γ " = $5C_2X_f\bar{14}$, where X_f is a fast pulse derived from the crystal output. If a gamma ray followed a μ stop within 0.5×10^{-6} sec (approximately three lifetimes of negative muons in copper), the spark chambers were triggered and photographed. At the same time, a *slow* pulse from the NaI crystal, X_s , and dynode pulses from counters 3, 4, and 5 were photographed on appropriate oscilloscope traces. Measurement of the pulse height of the slow pulse X_s gave information on the gamma-ray energy, and time information was obtained by measuring the separation $t_{\mu\gamma}$ of pulses 3 and 5.

In the normal operation of the synchrocyclotron, there are about 200 beam bursts per second with a duration of $150 \mu\text{sec}$ each, giving a duty factor of about 30. With the help of a rotating internal target it was possible to increase the duration of individual bursts to ~ 1.5 msec, reducing the duty factor to 3. The target which accomplished this "stretching" is shown in Fig. 4 and consisted of eight prongs of Steatite mounted on a

rotating shaft placed tangent to the proton beam. The dee rf voltage was cut off when the proton beam had reached a given radius. While the proton beam "coasted" at that radius in the magnetic field, the rotating target was swept slowly through the beam with the help of a synchronized motor. The target phase and rf cutoff time were adjusted to give maximum "stretched" beam. About 70% of the total beam appeared in this "stretched" portion, while the remainder appeared as a narrow "prompt" beam pulse which preceded the "stretched" beam pulse. With suitable gating it was possible to count only during the "stretched" beam pulse.

Counting only during the "stretched" beam pulse, an average of 1200 negative muons per second were stopped inside the five Cu plates of the SC1. Approximately 18.7% of the stopping particles were pions, as estimated from a range curve. Electrons did not con-

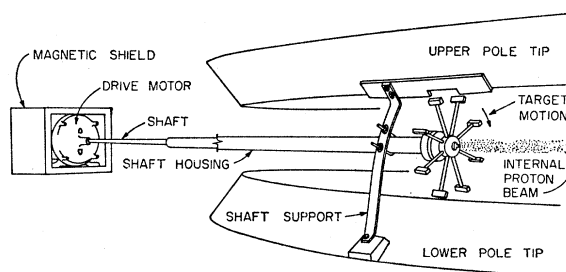


FIG. 4. Beam stretching apparatus. The radius of the spoke wheel is 4 in. and the ceramic knobs at the ends of the spokes are $1 \times \frac{1}{2} \times \frac{1}{2}$ in. The wheel revolved 25 times each second.

tribute to the stop count because of the anticoincidence of C_1 .

Counters used in the experiment are listed below:

1. 5×5×0.25-in. plastic scintillant,
2. 5×5×0.25-in. plastic scintillant,
3. 5.25×5.25×0.25-in. plastic scintillant,
4. 10×10×0.375-in. plastic scintillant,
5. 8×8×0.25-in. plastic scintillant,
- C_1 . 6×6×1-in. water Čerenkov counter,
- C_2 . 8×8×1-in. Lucite Čerenkov counter,
- X. 8 diameter×8-in. thick NaI crystal.

All the counters except the NaI crystal were viewed by RCA 6810-A photomultiplier tubes, through Lucite light pipes. The water Čerenkov counter C_1 was made of a Lucite frame with 0.005-in. aluminized Mylar windows, and viewed by photomultiplier tubes at each end.

The copper spark chamber was constructed with 0.109-cm-thick Cu plates and 0.048-cm-thick Al plates. The chamber consisted of nine plates, five of Cu and two plates at each end which were Al. All plates were spaced with 0.25-in.-thick Lucite frames which served to provide an air-tight enclosure, and windows for viewing the chamber. The sensitive area of the chamber was 8×8 in. and the thickness of copper was 4.85 g/cm². The lead spark chamber was an exact replica of the copper chamber, with the copper replaced by lead plates each 0.104 cm thick and made of 94% lead and 6% antimony (by weight). Antimony was added to make the plates rigid. The five lead plates constitute a total of 5.66 g/cm² of Pb (and Sb). The chambers were filled with a commercially available mixture of 90% Ne and 10% He at slightly above atmospheric pressure. Alternate plates of each chamber were joined together and connected separately to ground and two banks of 2500 pF condensers charged to 10 kV. Both of these condenser systems were discharged through the spark chamber gaps by a single 5C22 thyratron. The intrinsic delay in this triggering system was 150 nsec.

In the course of the experiment the two spark chambers were placed on either side of counter 4. With the help of a mirror, 90-deg stereoviews of both chambers were photographed through a spherical plastic field lens, with a camera positioned at the focal length of the field lens ($f=84$ in.). The whole spark chamber assembly was put inside a metal (aluminum and copper) box to keep the chamber discharge from interfering with the electronics. A special check was made to ensure that the spark discharge had no influence on the NaI crystal pulse height as recorded on the oscilloscope. The clearing fields of the chambers were 15.7 V/cm and the sensitive time was approximately 1.5 μ sec. The average efficiency of an individual gap was 97%.

The crystal was protected with an aluminum can 0.063 in. thick. The entire surface, except for those areas occupied by three 3-in.-diam windows, was

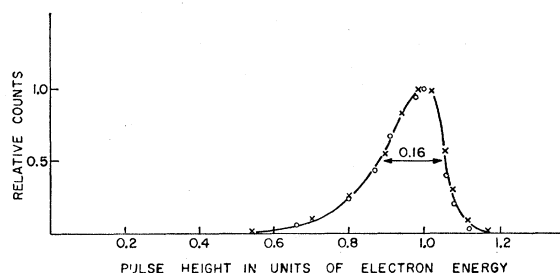


FIG. 5. Typical resolution curve for the NaI crystal.

covered with Al_2O_3 reflector. The crystal was viewed with three 3-in.-diam photomultiplier tubes (Dumont Type 6363) through Vycor windows.

The energy resolution of the crystal was measured using high-energy electrons coming from the conversion of π^0 decay gamma rays in the walls of a channel in the cyclotron shielding. With the help of a bending magnet it was possible to select electrons with energies from 40 to 200 MeV. A typical pulse-height spectrum is shown in Fig. 5. We found that the peak pulse height was a linear function of the electron energy and that the resolution remained constant at about 16% (full width at half-maximum) over the energy range of interest. The curve shows a characteristic deviation from a Gaussian.

The NaI crystal provided two pulses used in the electronics: (1) a fast anode pulse X_f clipped to 50 nsec, used in fast coincidence with counters 5 and C_2 to define a " γ " and (2) a slow pulse X_s , 2 μ sec in length, coming from the ninth dynode, used in the analysis of pulse height. With the high voltage set at 1100 V, the slow pulse was not saturated for gamma rays of energy up to 150 MeV. At this high voltage, the fast pulse was large enough to trigger the coincidence circuit for energies greater than approximately 14 MeV. This lower limit introduced a bias in detecting the gamma rays in the NaI crystal, since energy deposits in the crystal less than 14 MeV were not detected. This effect is seen in the decay electron spectrum (Fig. 7). The slow NaI pulse was routed to a multichannel pulse-height analyzer, in addition to being displayed on an oscilloscope. Linearity of the system was checked on the analyzer and on the scope with a pulse generator and with gamma-ray sources of known energy. The absolute energy calibration was made using gamma rays from a Pu-Be source ($E=4.43$ MeV), and also by minimum ionizing mu mesons from cosmic rays. In addition, these calibrations were checked by the observation of the electron energy spectrum from μ^- decays as discussed below.

C. Electronics

Figure 6 shows a block diagram of the electronic arrangement used in the experiment. All the coinci-

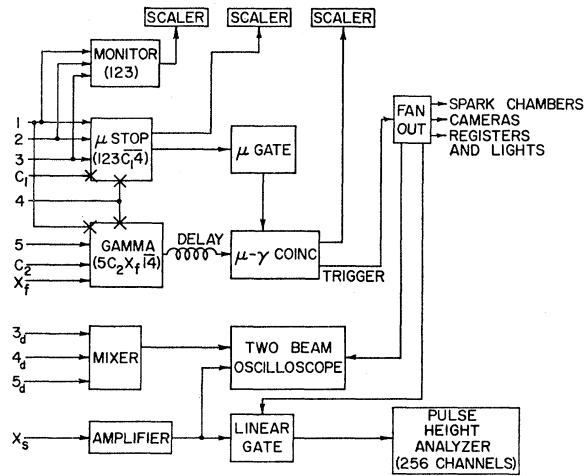


FIG. 6. Simplified electronic logic block diagram.

dence circuits were of the Garwin type,²⁰ of resolving time of approximately 20 nsec. The “μ stop” and the “γ,” and consequently the “events” were recorded only during the “stretched” beam pulse. The delayed fast output of the μ-stop coincidence circuit generated a gate approximately 5 μsec in width. The μ gate and the fast output of the “γ” circuit were fed into the “event” coincidence circuit. An event was recorded if a μ stop was followed by a γ in a time interval from 36 to 480 nsec after the time of the μ stop. The 36-nsec delay was introduced to avoid “prompt” events for which the γ and μ-stop pulses are in time coincidence ($t_{\mu\gamma}=0$). Dynode pulses, separated by suitable delays, from counters 3, 4, and 5 were displayed on an oscilloscope (Tektronix 555) with a sweep speed of 100 nsec/cm, and a total sweep time 1 μsec. The slow pulse of the NaI crystal was displayed on a separate sweep (sweep speed 100 nsec/cm).

To avoid confusion in registering the information for each event, it was convenient to introduce a dead time into the triggering system with the result that after each event trigger there was an interval Δt during which another trigger would be ignored. Correspondingly, the number of μ stops, N_{μ}' , which should be counted as effective during the run is related to the actual number N_{μ} recorded by the scalars by $N_{\mu}' = N_{\mu}h$. The factor h , which varied between 0.90 and 0.99, is determined by the interval of time Δt and the observed rate of events.

III. DATA AND ANALYSIS

A. Data

Various kinds of data were taken to provide information needed in the analysis. The triggering arrangements are described briefly below.

(1) $\mu\gamma$ data; the principal data of the experiment.

The triggering arrangement has been already explained in detail in Sec. II.

(2) $\mu^+\gamma$ data; as will be discussed later these data were collected in an attempt to estimate the correction to the $\mu\gamma$ “events” arising from external bremsstrahlung produced by decay electrons. The triggering arrangement was the same as that of (1) above.

(3) μ^- and μ^+ stops; the chambers in this case were triggered by μ stops (123C₁4). The pictures gave information on the range of muons, and the profile of the muon beam.

(4) μ^-e^- data; these data were taken to study the energy and time distribution of the muon decay electrons and thus provide an over-all check on the operation of the experiment. An event was defined by a coincidence of a μ gate generated by a μ stop (123C₁4) and an electron (5C₂X_f1). The μ^-e^- trigger was therefore the same as the $\mu^- \gamma$ trigger (1), but with 4 removed from the “γ” circuit.

(5) μ^+e^+ data; the purpose of taking these data was similar to that of (4) above. The triggering arrangement was the same as that of (4).

The number of stopped muons in each case are listed in Table I.

TABLE I. Number of stopped particles for different triggering modes.

Type of trigger	Number of stopped particles
$\mu^- \gamma$	3.38×10^8
$\mu^+ \gamma$	1.23×10^8
μ^- stops	4.33×10^8
μ^+ stops	5.28×10^8
$\mu^- e^-$	0.54×10^8
$\mu^+ e^+$	0.14×10^8

Spark chamber pictures taken with a μ stop as the trigger showed that the stopping distribution was fairly uniform over the last four copper plates. Inspection of these pictures shows that out of all μ-stop triggers, 60.5% are in the five copper plates, 12.5% are in other parts of the spark chamber, and 27.0% show no visible track. The μ-stop triggers with no visible track in the spark chamber are presumably due to particles stopping in counter 3, or to particles which scatter from counter 3 and stop elsewhere, thereby missing 4.

B. Analysis

(i) μ^-e^- Data

Candidates for μ^-e^- decay were required to show a continuous track which suffers a break in SC1 of at least 10 deg in either stereoview. Since the incident beam was at 45 deg with respect to the copper plates SC1 and the γ telescope was perpendicular to these plates, the angle between the decay electron and the

²⁰ University of California Lawrence Radiation Laboratory Report, UCRL 3307 Rev. (unpublished).

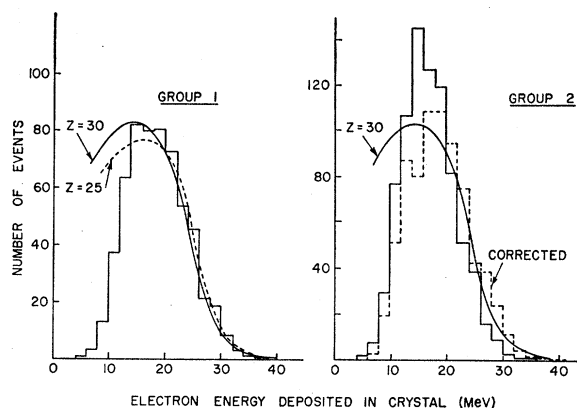


FIG. 7. Decay electron spectra. Group 1: Extension of electron's direction intersects bottom face of crystal. Group 2: Extension of electron's direction does not go through bottom face of crystal.

incident muon as seen from the "side" was in most cases near 45 deg. By "side" view we shall mean the view of the chambers seen from the direction perpendicular to the paper in Fig. 3. The other view which was reflected by a mirror and is perpendicular to the "side" view is called the "top" view. Events were rejected if: (1) the electron track stopped in SC2; (2) there was more than one track present in either SC1 or SC2; (3) counter 3 pulse appeared more than once on the trace; (4) counter 4 pulse was missing. The criteria (1), (2), and (3) resulted in a combined rejection of less than 1%. Criterion (4) did not in fact restrict the selection since all events showing the μ -e decay track configuration displayed the desired counter 4 pulse.

For the 2650 remaining "good" events, the NaI pulse heights and the time intervals $t_{\mu e}$ were measured. In obtaining the crystal pulse height distribution, the events were separated into two groups according to the directions of the electron tracks. Group 1 consisted of those events in which the extrapolated line of the electron track was inside the crystal and passed through its bottom. Group 2 consisted of the remaining events. The results are shown in the histograms of Fig. 7, where each event is represented by a rectangle of constant area centered at the measured pulse height, with base equal to 5 MeV (the estimated error in measurement of pulse heights). The ordinates of the histogram correspond to the sums of the rectangular areas associated with successive 2-MeV intervals. The expected pulse-height distribution was computed using the theoretical decay electron spectrum given by Huff,²¹ modified by the finite energy resolution of the NaI crystal and taking into account the ionization loss of the electrons before reaching the crystal. Computations were performed for nuclei of $Z=25$ and $Z=30$.

The pulse-height distribution for events in group 1,

taken above the lower cutoff energy of 14 MeV, shows excellent agreement with the computed distribution for $Z=30$, thus giving a good indication of the correctness of the energy calibration. For events of group 2, part of the shower produced by an electron may not be completely contained in the NaI crystal. The resulting pulse heights are expected to be smaller on the average than those for electrons of the same energy in group 1. As a way of correcting for this effect, we have tried to augment all pulse heights for the group 2 events by a fixed ratio, adjusting the ratio to give the best agreement with the pulse-height spectrum for group 1. The dashed histogram of Fig. 7, obtained through a 10% increase of all group 2 pulse heights, shows that the correction is satisfactory. On this basis we have made a similar correction in the subsequent analysis of the radiative capture events.

Figure 8(a) shows the time distribution of decay electrons obtained by measuring the time $t_{\mu e}$ between the μ stop and the electron. The dashed line includes a correction for the finite width of the μ gate and is obtained from the experimental points by adding an estimated number of events with $t_{\mu e} \geq 480$ nsec. The decay curve shows agreement with the disappearance rate of muons in copper ($\lambda = 5.92 \pm 0.02 \mu\text{sec}^{-1}$) measured by Eckhause *et al.*²² The detection efficiency at the beginning of the gate varied due to the time jitter in starting the gate with respect to the time of the μ stop. This effect is indicated by the slight drooping seen at the beginning of the decay curve.

(ii) $\mu^- \gamma$ and $\mu^+ \gamma$ Data

Candidates for these events were first selected from the spark chamber pictures and were subsequently considered eligible only if the oscilloscope traces met cer-

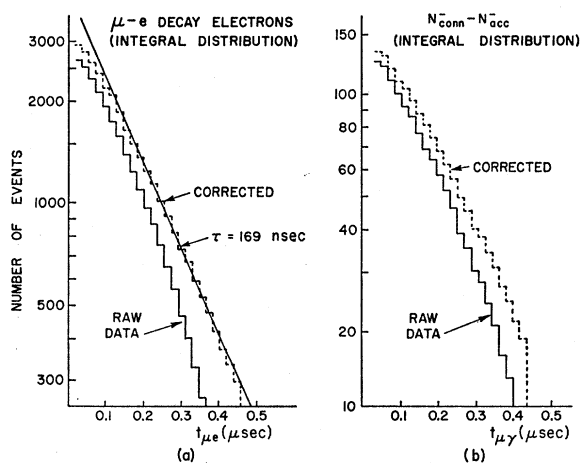


FIG. 8. Event time distributions. (a) Decay electrons. (b) Connected gamma events (with accidental background subtracted).

²¹ R. W. Huff, Ann. Phys. (N. Y.) **16**, 288 (1961).

²² M. Eckhause, A. Filippas, R. B. Sutton, R. E. Welsh, and T. A. Romanowski, Nuovo Cimento **24**, 666 (1962).

tain requirements. In scanning the spark chamber pictures, μ stop and γ were defined by track configurations having the following characteristics:

μ stop: The sparks in SC1 show that a particle entered along the beam direction (approximately 45 deg with respect to the plates on the side view and 90 deg on the top view). The track must stop in one of the five Cu plates, and, when extrapolated back, pass through counter 3.

" γ ": The sparks in SC2 indicate a charged particle or a pair originating in one of the lead plates and going toward the crystal unaccompanied by any charged particle coming from SC1.

Defining a track by at least two sparks, there were three kinds of " γ ":

(i) Y type: A single track at the beginning which splits into two after passing through some material.

(ii) V type: A pair of tracks emerging from a common point in a lead plate.

(iii) Single-track type: This type shows only a single track.

The scanners were instructed to choose all pictures showing a " γ " in SC2 whether or not a μ stop was present in SC1. The data recorded for each such picture are: the coordinates of the μ stop if present; the coordinates of the point of conversion; and the angles between each leg of the pair and the z axis defined as the line perpendicular to the plates of the spark chambers.

Events were rejected for one or more of the following reasons:

(1) There was more than one track in SC1. There were 28 pictures (3% of the total) with two μ stops. Five additional pictures showed, besides one μ stop, an extra track which did not satisfy the μ -stop criterion.

(2) A track in addition to " γ " was observed in SC2. Three cases were observed for pictures with a visible μ stop and two for those with no visible μ stop. This corresponds to 0.3% and 0.6% of the total in each category, respectively.

(3) Two pulses from the counter 3 were present on the oscilloscope trace. Eleven cases ($\sim 1\%$ of the total) and five cases ($\sim 1\%$) were observed for events with visible and nonvisible μ stops, respectively.

(4) A pulse from the anticoincidence counter 4 was present. One such picture was found in each μ -stop category. The numbers of events selected according to the above scanning rules are listed in Table II below. The $\mu^+\gamma$ events scanned with same rules are also listed.

TABLE II. Scanning table selection of $\mu^-\gamma$ and $\mu^+\gamma$ events.

Type of event	$\mu^-\gamma$	$\mu^+\gamma$
Total No. μ stops	3.38×10^8	1.23×10^8
Visible μ stop	2.05×10^8	0.79×10^8
Y -type " γ "	223	9
V -type " γ "	507	43
Single-track type " γ "	109	116

Since evidence will be presented later at the end of this section indicating that the single-track type " γ "'s are almost all accidentals, we shall leave them out at this point and restrict the discussion to events of the Y or V types which may be interpreted as visible pairs from gamma-ray conversion.

The main problem in the analysis of the data lies in making a spatial selection of the events. Because of the large effect of multiple scattering in the lead plates, it is not possible to directly infer the direction of the gamma ray from the direction of the electron and positron tracks as they are seen in the spark chamber pictures. It is therefore necessary to decide on some geometrical criterion for accepting an observed pair in SC2 as being causally connected with an observed μ stop in SC1. If a photon of a certain energy is converted to a pair inside a lead plate, the electron and positron will emerge from the plate in directions which are in general different from the original direction of the photon. The two angles θ_1 and θ_2 between the direction of the incident photon and that of each component of the pair will show a distribution characteristic of multiple scattering. In scanning the spark chamber pictures, the direction of each leg of the pair is defined by the first two sparks after the point of conversion. The electrons which produce these sparks suffer multiple scattering not only in the plate where the photon was converted, but also in the following lead plate. The direction of the electron measured in the spark chamber picture is therefore a result of compounding multiple scattering angles in each of the two plates mentioned above. To choose a suitable acceptance criterion, it is necessary to have prior knowledge of the distribution in the angles θ_1 and θ_2 . This was obtained with the help of a Monte Carlo calculation which followed the histories of gamma rays and the pairs into which they convert. For each incident gamma-ray energy E_γ , it was possible in this way to define a restricted region of acceptance in the θ_1, θ_2 plane, depending on the gamma-ray energy, which should contain all but a very small fraction of the pairs. If the θ_1, θ_2 for a given experimental $\mu\gamma$ event fell into the associated region of acceptance, it was accepted as having a possible connection between the μ stop and the γ . The regions of acceptance were triangular domains defined by $\theta_1 + \theta_2 \leq \theta_0$, where θ_0 is a function of E_γ , and were large enough to include approximately 95% of the connected events and yet small enough to reject a large part of the accidental or unconnected events. E_γ for each event was determined from the pulse height of the NaI crystal supplemented by the ionization loss suffered by the members of the pair in traversing the material intervening between the point of conversion and the surface of the crystal.

Requiring the $\mu\gamma$ events to fall in the appropriate (θ_1, θ_2) regions reduced the number of Y - and V -type " γ " events (with visible μ stops) from the 730 listed in Table II to 156 "connected" events. From these 156

TABLE III. Summary of events and accidentals.

	μ^-			μ^+		
N_{μ}'	3.05×10^8			1.20×10^8		
v	0.61 ± 0.03			0.64 ± 0.03		
f	0.924 ± 0.007			0		
g	0.65 ± 0.03			0.177 ± 0.005		
	Group 1	Group 2	Total	Group 1	Group 2	Total
N_{conn}	49	107	156	26	13	39
N_{acc}	8.4 ± 1.0	22.9 ± 3.1	31.3 ± 3.3	1.5 ± 0.2	0.3 ± 0.1	1.8 ± 0.2
N_{IB}	24.5 ± 8.1	75.7 ± 10.5	100.2 ± 13.6			

events it is essential to subtract an estimate of the number in which the “ γ ” and μ stop are not causally related but only accidentally connected. Random “ γ ”’s may be preceded by unrelated μ ’s stopping in the appropriate time interval to satisfy the electronic requirement for $\mu\gamma$ events, giving rise to a certain number of random $\mu\gamma$ ’s. Of these a fraction, let us say $(1-\alpha)$, will appear geometrically unconnected, while the remaining fraction α will appear connected. The number of accidentals, i.e., number of random $\mu\gamma$ ’s which appear connected, will therefore be a fraction $\alpha/(1-\alpha)$ of the number of randoms rejected as not satisfying the geometrical requirements imposed by the region of acceptance, (θ_1, θ_2) . Calculation of α is a geometrical problem. Taking the experimentally rejected $\mu\gamma$ events as providing a sample of typical random “ γ ”’s, it is possible, by Monte Carlo methods, to calculate the average probability that a μ will stop in such a region of the Cu plates that the resulting geometrical configuration will give a $\mu\gamma$ with θ_1 and θ_2 in the proper region. The difference between the number of “connected” events and the accidentals is then the “net effect.”

We define the following quantities (a superscript $-$ or $+$ will be used to refer explicitly to the case of μ^- or μ^+ , respectively):

N_{μ}' is the effective number of μ stops. (See discussion of dead time circuit above; Sec. II C.)

v is the fraction of visible μ stops out of the total μ -stop triggers. $v^- = 0.61 \pm 0.03$ and $v^+ = 0.64 \pm 0.03$.

N_{IB} is the number of radiative capture events observed. (IB is for “internal bremsstrahlung.”) N_{IB} will be defined below.

N_{conn} is the number of events for which the “ γ ” and μ stop satisfy the criteria of “connectedness.”

N_{acc} is the number of accidentals estimated according to the method discussed above.

f is the fraction of muons undergoing nuclear capture in Cu. For negative muons in Cu, the total muon disappearance rate is $\lambda_{\text{tot}} = (5.92 \pm 0.02) \mu\text{sec}^{-1}$.²² The capture rate is given by $\lambda_{\text{capt}} = \lambda_{\text{tot}} - \lambda_{\text{decay}}$. For λ_{decay} we use the decay rate of free muons,²² $\lambda_{\text{decay}} = (0.4541 \pm 0.008) \mu\text{sec}^{-1}$, neglecting the small correction due to the fact that the muon is actually bound in a Bohr

orbit. This gives $\lambda_{\text{capt}} = (5.47 \pm 0.02) \mu\text{sec}^{-1}$. Therefore $f^- = \lambda_{\text{capt}}/\lambda_{\text{tot}} = 0.924 \pm 0.007$. Of course $f^+ = 0$.

g is the fraction of events occurring within the time of the μ gate, and is obtained experimentally from the μ - e decay curve. g was computed using the experimentally measured numbers of μe decay events. This procedure takes into account the decline in efficiency at the beginning of the gate due to jitter, which was mentioned earlier. This gives $g^- = 0.65 \pm 0.03$. In the case of positive muons, the uncertainty in g^+ is small since $1/\lambda^+ = 2.20 \mu\text{sec}$ is large compared with the μ gate width. We find $g^+ = 0.177 \pm 0.005$.

A summary of these quantities is contained in Table III.

For the same reasons discussed earlier in the classification of the crystal pulses from μe decay electrons, it was convenient to separate the radiative capture events into two groups, 1 and 2, according to the following criteria: To qualify for group 1 an event was required to show that both legs of the pair resulting from the γ -ray conversion entered the crystal, and that at least one of them, when extrapolated, passed through the lower surface of the crystal. Group 2 contained the remaining events. In most cases both legs of the pair entered the crystal.

We now compute N_{IB} , the total number of radiative capture events observed. For the $\mu^- \gamma$ events the difference $N_{\text{conn}}^- - N_{\text{acc}}^-$ includes counts from genuine radiative captures as well as from external bremsstrahlung by decay electrons. The net effect observed for $\mu^+ \gamma$, $(N_{\text{conn}}^+ - N_{\text{acc}}^+)$, can be attributed entirely to the external bremsstrahlung and one may attempt to use this information to make a subtraction.

Although the electron spectrum for μ^+ differs substantially from that of μ^- near the upper end of the spectrum, we have assumed that the corresponding external bremsstrahlung spectra do not differ as much. Figure 9 indicates the expected energy variation of the detection efficiency for gamma rays in groups 1 and 2 as obtained in the Monte Carlo calculations of Sec. IV below. In the energy region below 50 MeV, where the subtraction of external bremsstrahlung is important, the detection efficiency of the apparatus is not flat but is varying rapidly. In addition, the detection efficiencies

TABLE IV. The differential and the integral distribution of radiative capture events.

Pulse-height interval (MeV)	Group 1	N_{IB}^a Group 2	Total	Pulse-height E (MeV)	$N_{IB}(E)^b$ Total
5-10	-0.5 ± 1.9	-0.2 ± 1.0	-0.7 ± 2.1	5	100.5 ± 15.4
10-15	-0.1 ± 3.5	7.9 ± 3.0	7.8 ± 4.6	10	101.2 ± 15.2
15-20	3.0 ± 3.5	14.2 ± 4.3	17.2 ± 5.5	15	93.4 ± 14.5
20-25	2.2 ± 3.1	13.8 ± 4.9	16.0 ± 5.8	20	76.2 ± 13.1
25-30	4.4 ± 2.4	14.3 ± 4.6	18.7 ± 5.2	25	60.2 ± 11.7
30-35	5.5 ± 2.5	8.7 ± 4.0	14.2 ± 4.7	30	41.5 ± 10.3
35-40	4.6 ± 2.3	5.2 ± 4.4	9.8 ± 5.0	35	27.3 ± 9.4
40-45	0.4 ± 1.0	1.5 ± 0.8	1.9 ± 1.3	40	17.5 ± 7.9
45-50	0.6 ± 1.2	5.1 ± 2.6	5.7 ± 2.9	45	15.6 ± 7.7
50-55	1.4 ± 1.2	0.3 ± 1.0	1.7 ± 1.7	50	9.9 ± 5.5
55-60	1.1 ± 1.1	0.7 ± 1.1	1.8 ± 1.6	55	8.2 ± 4.2
60-65	0.0 ± 0.0	0.4 ± 1.4	0.4 ± 1.4	60	6.4 ± 3.4
65-70	0.0 ± 0.0	2.4 ± 1.9	2.4 ± 1.9	65	6.0 ± 3.1
70-75	0.0 ± 0.0	0.0 ± 0.0	0.0 ± 0.0	70	3.6 ± 2.4
75-80	0.8 ± 0.9	1.5 ± 1.5	2.3 ± 1.8	75	3.6 ± 2.4
80-85	1.2 ± 1.1	0.1 ± 1.2	1.3 ± 1.6	80	1.3 ± 1.6
Total	24.6 ± 8.1	75.9 ± 13.1	100.5 ± 15.4		

^a Net number of inner bremsstrahlung events calculated according to Eq. (4) for each of the pulse-height intervals of column 1.

^b Net number of inner bremsstrahlung events with pulse height greater than or equal to E .

for gamma rays from the two groups can be expected to be different, the efficiency reaching its maximum at somewhat higher energies for group 2. This is due to the fact that, for events in group 2, the energy deposited in the crystal is less and the corresponding pulse height lower, thus making those events more difficult to detect. We believe that these effects are reflected in Table III in the relative numbers of connected events. As can be seen, the ratio of connected events in group 1 to those in group 2 is 0.49 for μ^- while it is 1.9 for μ^+ . In any case these considerations do not play a large role in the determination of a branching ratio, as will be seen in Sec. IV, since they are important only in the lower portion of the gamma spectrum which was detected by the apparatus.

For a total of $N_{\mu^+} \nu^-$ effective negative μ stops with a visible track in SC1, the associated number of decay electrons falling within the μ gate is equal to $N_{\mu^+} \nu^- g^-$

$\times (1 - f^-)$, in the notation defined previously. Similarly, the number of decay positrons is $N_{\mu^+} \nu^+ g^+$. Since the external bremsstrahlung processes must be proportional in number to the decay electrons, we may write for the net number of μ^- radiative capture, or internal bremsstrahlung, events:

$$N_{IB} = (N_{conn}^- - N_{acc}^-) - r(N_{conn}^+ - N_{acc}^+), \quad (3)$$

where

$$r = [N_{\mu^+} \nu^- g^- (1 - f^-)] / N_{\mu^+} \nu^+ g^+,$$

$r = 0.66 \pm 0.08$, for the data of Table III. In this subtraction procedure the numbers N_{IB} , N_{conn} , etc., may refer to events falling into any classification according to gamma-ray energy. The N_{IB} may therefore represent, for example, the integral number of radiative capture events with observed pulse height in the NaI crystal above a certain limit, or the differential number with pulse height in a certain interval. The results of this analysis are contained in Table IV and in Fig. 10.

It may be remarked that the ratio of internal bremsstrahlung events in group 2 to those in group 1 is 3.1 ± 1.1 , which is consistent with the value of 3 obtained from the expected detection efficiencies shown in Fig. 9.

The time distribution of the net effect is obtained from that of the "connected" events after subtracting the accidentals which are assumed to be uniformly distributed over the observed range. The integral time distribution histogram is shown in Fig. 8(b) along with the results from $\mu^- e^-$ decay electrons. The graph shows that the time distribution of events is consistent with that expected from the experimentally observed muon disappearance rate in Cu.²² Figure 11 gives the differential time distributions for the four categories: net effect ($N_{conn}^- - N_{acc}^-$), single track type " γ ," rejected

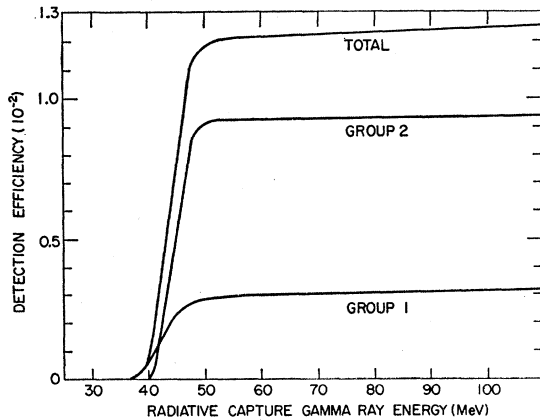


FIG. 9. Efficiencies for detection of gamma rays as computed by a Monte Carlo program.

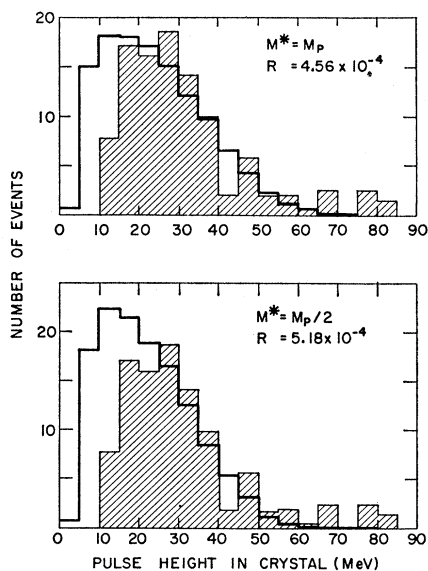


FIG. 10. Experimental and fitted radiative capture spectra for two choices of the effective mass used in the Fermi-gas-model calculation. The hatched area represents the observed data; the heavy solid line represents the theoretical spectrum which fits the data best. The errors in the observed data are statistical (including contributions from background subtraction) and are given in Table IV.

pairs (N_{rej}^-), and pairs with no visible stop. The calculated mean lives are:

- | | |
|--|--------------------|
| (1) $N_{conn} - N_{acc}$ | 175 ± 14 nsec; |
| (2) the single-track type | 194 ± 14 nsec; |
| (3) the rejected pairs | 234 ± 10 nsec; |
| (4) the pairs with no visible μ stop | 235 ± 14 nsec. |

For the events (1) this mean life compares favorably with 169 ± 0.5 nsec which is the mean life of μ^- in copper.²² For an accidental or uniform time distribution, we would expect to get a mean life of 222 nsec, which corresponds to the middle of the gate. We conclude that (3) and (4) are accidental.

The time distribution for the single-track type events is not obviously accidental in nature but contains a relatively large accidental component. The origin of the single-track-type " γ "'s is not known. One possibility is that they may be associated with electrons produced by background gamma rays in the NaI crystal. Such electrons would give pulses in the NaI crystal, the Čerenkov counter C_2 and the counter 5 and could stop in one of the lead plates of SC2. The distribution of pulse heights from counter 5 indicated that the majority of the single-track type " γ "'s are actually due to single particles rather than pairs. We can expect, therefore, that neglecting such " γ "'s does not result in an appreciable loss of good events.

IV. CALCULATION OF THE BRANCHING RATIO

The branching ratio is obtained by comparing the results of the analysis of Sec. III with an *expected* crystal pulse-height distribution. The observed spectrum contains contributions from pairs created over the entire volume of the lead spark chamber SC2, and whose members have therefore lost varying amounts of energy in addition to being multiply scattered, before entering the crystal. The expected spectrum is found by operating on a theoretical radiative capture gamma-ray spectrum with a Monte Carlo program. Photons with energy chosen according to the theoretical spectrum are assumed to emerge isotropically from a point picked according to the observed μ^- -stop distribution. In following the histories of these photons, proper account is taken of conversion efficiency in the lead plates, multiple scattering of the electron and positron of the pair, ionization loss, and the energy resolution of the crystal. We have neglected radiative energy loss of the electrons and positrons in their journey towards the crystal since most of this goes forward and is included in the pulse registered by the crystal. In the course of calculation, events will fall into the two categories, group 1 and group 2, mentioned previously. The same method used to combine these groups for the decay electron spectrum, is applied automatically during calculation, so that the resulting expected spectrum can be directly compared to the observed spectrum gotten by adding the two groups together. The particular theoretical

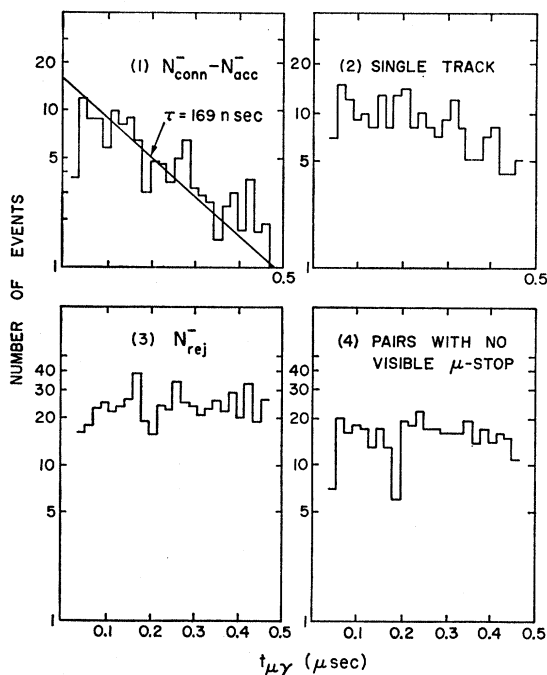


FIG. 11. Time distributions for various types of " γ " configurations.

spectrum used in this calculation is discussed in Appendix 1.

The branching ratio, R , is then calculated as follows: Let $N_{IB}^{exp}(E)$ be the number of observed events whose crystal pulse height falls in an interval ΔE about E . Let $N_{IB}^{MC}(E, R^{MC})$ be the corresponding number obtained through the Monte Carlo calculation, using R^{MC} as a trial value for the branching ratio. Note that for any given R^{MC} , the calculated spectrum is always normalized to the number of mu stops responsible for the observed spectrum. At this point we also introduce the correction factor which takes account of the pion contamination of 18.7% already mentioned in Sec. II. We then form the chi-square from the numbers and their associated errors:

$$\chi^2(E_0, R^{MC}) = \sum_{E=E_0}^{E_{max}} \left[\frac{N_{IB}^{exp}(E) - N_{IB}^{MC}(E, R^{MC})}{\sigma(E)} \right]^2, \quad (4)$$

where $\sigma(E)$ is the error obtained by a proper combination of experimental errors and errors from the Monte Carlo calculation (the error from calculation is relatively small since a large number of trials was chosen). In Eq. (4) are included only data where the energy deposited in the crystal is larger than the cutoff E_0 . The results are then expressed in terms of this parameter. The value $R(E_0)$ of R^{MC} which minimizes χ^2 represents the best estimate for the branching ratio for a particular choice of E_0 . An error on $R(E_0)$ is assigned by calculating the likelihood function associated with χ^2 .

The theoretical spectrum depends upon the value taken for the effective nucleon mass (see Appendix 1). The calculations were performed for two values of this parameter: $M^* = M_p$ and $M^* = M_p/2$, where M_p is the

mass of the proton. Figure 12 shows the best values of R as a function of E_0 . For small E_0 the efficiency for detecting gamma rays is small and varies rapidly with energy. In estimating the branching ratio, care must be taken to choose an E_0 for which the detection efficiency is approximately constant. A safe lower bound in E_0 can be obtained from the electron data shown in Fig. 7. From there we choose a value of $E_0 \approx 15$ –20 MeV. This choice is not very critical since Fig. 12 shows that R does not change rapidly with E_0 . Using this value for E_0 and the data shown in Fig. 10, one arrives at a value for the branching ratio of

$$\begin{aligned} R &= 4.56 \pm 0.70, \quad M^* = M_p, \\ R &= 5.18 \pm 0.80, \quad M^* = M_p/2, \end{aligned} \quad (5)$$

where R is measured in units of 10^{-4} .

In Fig. 10 we have drawn expected pulse-height distributions for each of these branching ratios to be compared with the observed distributions of Table IV. It is evident that the deviation between the expected values and the observed values is large for energies below 15 MeV. This is in all likelihood due to the difficulties inherent in the Monte Carlo calculation when dealing with low-energy electrons for which theoretical estimates of the detection efficiency depend very sensitively on the details of the very large multiple scattering. At the high-energy end of the spectrum there is also a relatively large difference between expected and observed spectra. Table IV shows that, above a crystal pulse height of 65 MeV, 6 ± 3 events remain after the subtraction of accidental background (one event), out of the total number of 100 events. Although the statistical accuracy is poor, this number of high-energy events is surprising. According to the phase-space γ -ray spectrum, calculated in the Appendix, Fig. 14, we would expect the upper end of the spectrum to be depleted due to nuclear excitations. The effect is clearly indicated in Fig. 10 where the expected crystal pulse-height distribution shows very small values above 65 MeV compared to the observations. We have carefully examined these high-energy events and have been unable to reject them on the basis of any of our acceptance criteria. They must remain as events to be counted, possibly representing a background which, because of a fluctuation, was not removed by our sampling procedure for subtracting accidentals.

Another estimate of the branching ratio can be obtained by requiring that the total number of expected events with energy greater than E_0 be equal to the number of observed events above this energy. This procedure results in values for R which are comparable with those obtained from the least squares fitting procedure described above. For $E_0 = 15$ MeV, the following values of R are obtained:

$$R = 4.96 \pm 0.76, \quad M^* = M_p; \quad R = 5.49 \pm 0.85, \quad M^* = M_p/2.$$

Since the apparatus is sensitive only to the upper

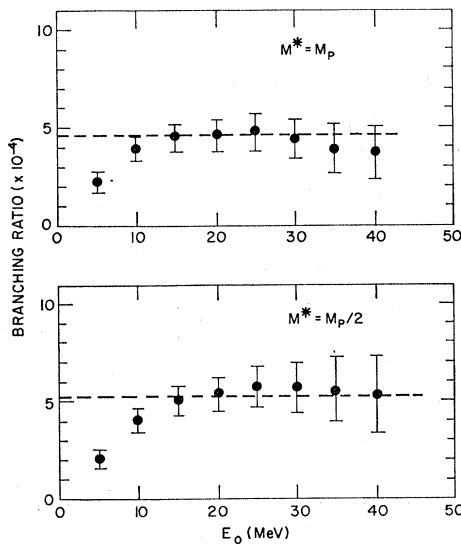


FIG. 12. Best values of branching ratio as function of crystal pulse height for two different values of effective mass used in Fermi-gas-model calculation.

portion of the gamma-ray spectrum, the branching ratio will depend strongly on the fraction of the total spectrum represented by this region. It may be helpful, therefore, to quote instead a partial branching ratio for the part of the γ -ray spectrum actually observed. Unfortunately, due to uncertainties involved in the passage from the point of origin of the γ ray to the crystal and due to the resolution of the crystal, it is not possible to uniquely correlate the measured pulse-height distribution with a portion of the capture γ -ray spectrum above a definite lower limit. Nevertheless, it is evident from the comparison in Fig. 10 of expected and observed pulse height distributions that the theoretical spectra used in the Monte Carlo calculations provide reasonable approximations to the general shape of the capture γ -ray spectrum above 50 MeV. We may, therefore, estimate an experimental partial branching ratio $R_p(E_\gamma)$ for μ^- capture leading to γ rays of energy larger than E_γ by integrating the theoretically assumed spectrum above E_γ choosing the scale factor as in Eq. (4), to give a best fit to the observed pulse-height distribution. In effect, this amounts to taking for $R_p(E_\gamma)$ the product of the "total" branching ratio R , obtained previously, Eq. (5), and the fraction of the theoretical spectrum above E_γ .

The resulting values for $R_p(E_\gamma)$ for $E_\gamma = 50$ and 60 MeV are given in Table V for each of the theoretical

using the efficiency shown in Fig. 9, and the data in Table IV. Events where the original gamma energy is larger than 50 MeV produce crystal pulse heights about 15 MeV or larger. Therefore we can write

$$N^{\text{exp}} = N_\mu' f_\mu v f g R_p \eta,$$

where N^{exp} is the number of observed events with pulse height larger than 15 MeV, f_μ is the fraction of stopping particles which are muons, η is the efficiency ($\eta \approx 1.2 \times 10^{-2}$ from Fig. 9), and all other quantities have been defined earlier. Inserting the values and solving for R_p results in $R_p = (0.85 \pm 0.14) \times 10^{-4}$. When this is compared to the partial branching ratios in Table V for 50 MeV, the agreement is seen to be quite good considering the approximate nature of this calculation.

V. EXTRAPOLATIONS OF THE RESULTS TO CAPTURE BY A PROTON AND ESTIMATION OF THE RATIO $g_P^{(\mu)}/g_A^{(\beta)}$

In order to use the present experiment to obtain information about the muon capture coupling constants, in particular the induced pseudoscalar constant, the effects due to nuclear physics must be unfolded from the experimental results. This is not a simple problem. Especially for the induced pseudoscalar coupling it is possible that the propagator for pions in the nucleus is seriously modified from what it would be in the case of μ capture by a single proton. Keeping this basic limitation in mind, we shall nevertheless attempt to estimate the branching ratio for radiative capture by a single proton on the assumption that in first approximation the principal effect of the nuclear structure is to reduce the phase space available to the neutrino and gamma ray in the final state, and thus to reduce the branching ratio. That is, we assume

$$R(A, Z) \approx k(A, Z) R(1, 1), \quad (6)$$

where $R(A, Z)$ is the radiative capture branching ratio for the complex nucleus (A, Z) , $R(1, 1)$ is the ratio for the proton and $k(A, Z)$ is a factor expressing the loss in phase space. Calculations of the phase space effects alone can be made with the help of a model of the nucleus as a condensed Fermi gas, with the capture matrix elements in effect replaced by constants. The procedure outlined in the Appendix gives, in the case of copper, $k = 0.61$ for $M^* = M_p$ and $k = 0.55$ for $M^* = M_p/2$. Rood and Tolhoek¹⁴ have attempted to take account of the explicit capture matrix elements in calculating the radiative and ordinary capture in the calcium 40 nucleus using the closure approximation. Their discussion includes the principal radiative capture diagrams, Fig. 2, and forms the basis of the estimate of $g_P^{(\mu)}$ given by Conversi *et al.*⁶ in the analysis of the calcium-40 experiment. Expressed in the form of Eq. (6), the equivalent values of k are in the same range as those given above, with a weak dependence on the magnitude of $g_P^{(\mu)}$.

TABLE V. Partial branching ratios.

E_γ (MeV)	$M^* = 938.2$ MeV	R_p (in units of 10^{-4}) $M^* = 469.1$ MeV	Conversi (Ref. 6)
50	1.20 ± 0.18	1.14 ± 0.18	
60	0.66 ± 0.10	0.56 ± 0.09	0.38 ± 0.04

spectra assumed. Also included in the table for purposes of comparison is the partial branching ratio for $E_\gamma = 60$ MeV which we have estimated from the experimental results of Conversi *et al.*⁶ in calcium-40, using the theoretical spectra of Rood and Tolhoek¹⁴ (Fig. 1 of Conversi's paper⁶). On this basis it appears that our measurement in copper shows the radiative capture process to be relatively more prominent than in calcium-40. This same conclusion can be drawn from a comparison of the total branching ratio for which Conversi *et al.*⁶ find a value of $(3.1 \pm 0.6) \times 10^{-4}$.

From the choice of E_0 , one can estimate the energy of the gamma rays (at their point of conversion) to which the apparatus was sensitive. One must remember that E_0 is the energy deposited in the crystal and that the electrons contributing to it could have originated in different parts of the lead chamber and have, therefore, lost varying amounts of energy. However, taking all this into account one can say that the apparatus was an efficient detector for gamma rays above about 50 MeV. A rough check of the partial branching ratio obtained above can be made directly from the data,

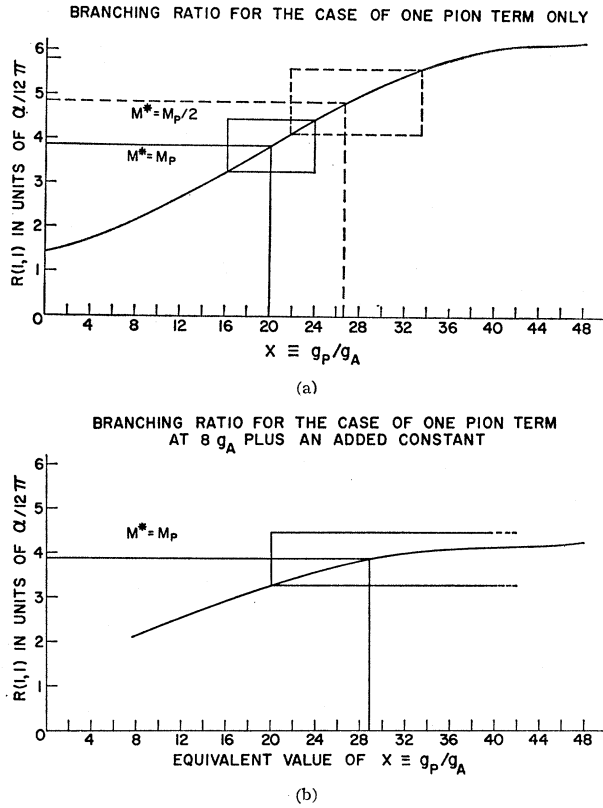


FIG. 13. (a) The branching ratio for protons as a function of the induced pseudoscalar coupling constant, when the matrix element contains only a single-pion exchange. (b) The branching ratio for protons as a function of the equivalent value of the induced pseudoscalar coupling constant, when the matrix element contains the one pion term plus an additional constant. Here, and also in Fig. 13(a), the results of this experiment extrapolated to protons using (6), are shown with rectangles to define errors.

Using the Fermi gas spectra of Fig. 14 to extrapolate from the observations to the branching ratios R for the entire gamma-ray spectrum, Eqs. (4) and (5), and taking the reduction factor k as above, we obtain estimates for $R(1,1)$ through Eq. (6). These estimates are now to be compared with theoretical calculations of $R(1,1)$ for different values of the μ^- coupling constants. We have used for this purpose the work of Manacher⁷ who has given a detailed consideration of the radiative capture for protons emphasizing especially the importance of the induced pseudoscalar interaction g_P . Figure 13(a) shows $R(1,1)$ as a function of the ratio $x = g_P^{(\mu)}/g_A^{(\beta)}$ taking the remaining coupling constants (in the notation of Ref. 8) equal to the presently accepted values for the universal Fermi interaction with conserved vector current²³ (in good agreement with the experimental capture rates in hydrogen¹ and helium²):

$$\begin{aligned} g_V^{(\mu)} &= 0.97 g_V^{(\beta)} = 0.98 \times 10^{-5} / M_p^2, \\ g_A^{(\mu)} &= g_A^{(\beta)} = -1.22 g_V^{(\mu)}, \\ g_M^{(\mu)} &= 3.7 g_V^{(\mu)}. \end{aligned}$$

²³ Scalar and tensor couplings are set equal to zero.

Only the ratios $g_A^{(\mu)}/g_V^{(\mu)}$ and $g_M^{(\mu)}/g_V^{(\mu)}$ together with $g_P^{(\mu)}/g_A^{(\mu)} = x$, are needed. The resulting values for x are

$$\begin{aligned} x &= 20 \pm 4 \quad \text{for } M^* = M_p, \\ x &= 27_{-6}^{+7} \quad \text{for } M^* = M_p/2. \end{aligned}$$

These values for x are far in excess of the value 7 or 8 to be expected^{3,4} if the induced pseudoscalar interaction is due entirely to the exchange of a single pion coupling the $(\bar{\mu}p)$ current to the $(\bar{\nu}\mu)$ current by means of the pion decay interaction. Some reduction in our estimate of x would result from the fact that for the large x under consideration the gamma-ray spectrum at the upper end is enhanced over what is indicated by the purely phase-space spectrum of Fig. 14, thus reducing the calculated experimental branching ratio. An estimate of this effect shows that g_P/g_A is reduced for this reason from 20 ± 4 to 15 ± 3 or from 27_{-6}^{+7} to 19 ± 4 . In the analysis of the experiment on the radiative capture in calcium-40, Conversi *et al.*,⁶ give $g_P^{(\mu)} = (13.3 \pm 2.7) \times g_A^{(\beta)}$, a result smaller than ours. This is a reflection of the fact, evident from Table V, that according to their measurements the radiative capture in calcium-40 is relatively smaller than our results would indicate for copper.

It is difficult to believe that there can be a major error in the theoretical estimate of the single pion contribution to the induced pseudoscalar coupling for the μ^- capture by protons. Under the circumstances one may suppose that the naïve procedure used for going from the branching ratio in copper to the branching ratio for protons is to a large extent misleading. Alternatively, in an experiment such as this, badly limited by statistics, there is always the possibility that in spite of our careful screening of each event we have admitted a systematic background which escaped notice. If we take the large radiative capture rate seriously, it is of interest to consider a suggestion of Wolfenstein^{24,25} that the induced pseudoscalar interaction be modified to take account of possible additional terms Δg_P not associated with the single-pion propagator. The pseudoscalar form factor would then be expressible as

$$g_P = 8g_A[(m_\pi^2 + m_\mu^2)/(m_\pi^2 - q^2)] + \Delta g_P,$$

where the dependence on the square of the four-momentum transfer q^2 is largely confined to the single pion propagator. We have analyzed our results for $R(1,1)$, Eq. (6), on this basis, assuming for extrapolation purposes that the γ -ray spectrum is adequately represented by the phase space spectra of Fig. 14. Figure 13(b) shows $R(1,1)$ as a function of an equivalent ratio x defined in this case by

$$x_{\text{equiv}} = [g_P/g_A]_{(q^2 = -m_\mu^2)} = 8 + (\Delta g_P/g_A).$$

²⁴ L. Wolfenstein, Brookhaven National Laboratory Report BNL 837, p. 292, 1963 (unpublished).

²⁵ G. I. Opat, Phys. Rev. **134**, B428 (1964).

From this curve we obtain

$$x_{\text{equiv}} = 29_{-9}^{+10} \quad \text{for } M^* = M_p$$

or

$$\Delta g_P = (21_{-8}^{+10}) g_A.$$

The case where $M^*_p = M_p/2$ would result in a still larger value for Δg_p , greater than $40 g_A$, accompanied by equally large errors. This is to be compared with the result $\Delta g_P = (10.4 \pm 5.6) g_A$ obtained by Conversi *et al.*⁶ for a similar analysis of the calcium-40 experiment. In either case such large values of g_P appear to be in disagreement with the results of μ^- capture in hydrogen¹ and helium.²

ACKNOWLEDGMENTS

Many thanks are due to G. B. Yodh, P. Palit, and R. Carrigan for their most generous assistance during phases of this experiment. We would like to express our appreciation for many fruitful discussions with Professor L. Wolfenstein. We are also grateful to D. Gupta and D. Sashin for their contributions and to the film scanners, R. Barr and K. Painter, as well as to the entire cyclotron staff.

APPENDIX 1. GAMMA-RAY SPECTRUM ACCORDING TO THE FERMI GAS MODEL

The "theoretical" gamma ray spectrum used in the Monte Carlo calculations of Sec. IV is based on a Fermi-gas model for the initial and final nuclei and may be expected to represent in a reasonable fashion the effects of phase space and the exclusion principle in determining the spectral shape.

Using the notation of Kaplan *et al.*²⁶ who considered the corresponding problem for ordinary (nonradiative) muon capture, the total probability for radiative capture by the protons in a completely degenerate Fermi gas is proportional to the phase-space integral

$$J_{\text{rad}} = \int \frac{d^3k}{k} d^3p_r d^3p d^3q f(\mathbf{p}) [1 - g(\mathbf{q})] \times \delta(\mathbf{q} + \mathbf{k} + \mathbf{p}_r - \mathbf{p}) \delta(E_0 - k - p_r - Q), \quad (\text{A1})$$

where the symbols have the following meaning: \mathbf{p} is the momentum of a proton in the nucleus prior to capturing the muon, \mathbf{q} is the momentum of the resulting neutron in the final nucleus, and \mathbf{k} and \mathbf{p}_r are the momenta of the photon and neutrino, respectively. The factor $1/k$ puts in evidence the characteristic normalization which appears in the probability for photon emission. The functions $f(\mathbf{p})$ and $g(\mathbf{q})$ give the proton and neutron momentum distributions in the initial and final nucleus, the product $f(\mathbf{p})[1 - g(\mathbf{q})]$ serving to restrict the integration $d^3p d^3q$ to occupied proton states and unoccupied neutron states. In the Fermi-gas model,

²⁶ S. N. Kaplan, B. J. Moyer, and R. V. Pyle, Phys. Rev. **112**, 968 (1958).

$f(\mathbf{p})$ and $g(\mathbf{q})$ are taken as unity or zero according to whether the momenta \mathbf{p} and \mathbf{q} fall inside or outside the proton and neutron Fermi spheres, $p = p_0$ and $q = q_0$. Conservation of momentum and energy in the elementary absorption process are expressed by the restrictions imposed by the two delta functions:

$$\begin{aligned} \mathbf{p} &= \mathbf{q} + \mathbf{k} + \mathbf{p}_r, \\ E_0 &= k + p_r + Q, \end{aligned} \quad (\text{A2})$$

where Q is the excitation energy of the product nucleus and E_0 is the total available energy.²⁷ Assuming that the ground state of the product nucleus is obtained by the conversion of a proton on the Fermi surface $p = p_0$ to a neutron on the Fermi surface $q = q_0$, Q is defined by

$$Q = (1/2M^*)(q_0^2 - p_0^2) - (1/2M^*)(q_0^2 - p_0^2), \quad (\text{A3})$$

where M^* is the effective nucleon mass.

To find the gamma-ray spectrum it is necessary to carry out the integrations in (A1) over $d^3q d^3p d^3p_r$. This is a straightforward but rather lengthy calculation and we shall discuss only the general outline of the procedure.

Use of the momentum delta function results immediately in

$$J_{\text{rad}} = \int \frac{d^3k}{k} d^3p_r d^3p f(\mathbf{p}) [1 - g(\mathbf{q})] \times \delta[E_0 - \psi(\mathbf{p}, \mathbf{p}_r, \mathbf{k})], \quad (\text{A4})$$

where in $g(\mathbf{q})$ the neutron momentum is understood to be $\mathbf{q} = \mathbf{p} - \mathbf{k} - \mathbf{p}_r$, and

$$\begin{aligned} \psi(\mathbf{p}, \mathbf{p}_r, \mathbf{k}) &\equiv k + p_r + Q \\ &= k + p_r + (1/2M^*)\{(\mathbf{k} + \mathbf{p}_r)^2 - 2\mathbf{p} \cdot (\mathbf{k} + \mathbf{p}_r) \\ &\quad - (1/2M^*)(q_0^2 - p_0^2)\}. \end{aligned} \quad (\text{A5})$$

For performing next the d^3p integration, keeping \mathbf{k} and \mathbf{p}_r fixed, note that the integrand in (A5) may be written as the derivative of a step function:

$$\begin{aligned} f(\mathbf{p})[1 - g(\mathbf{q})]\delta(E_0 - \psi) &= (\partial/\partial E_0)\Theta(E_0, \psi) \\ \Theta(E_0, \psi) &\equiv 1 \text{ if } \begin{cases} \text{(i) } \psi(\mathbf{p}, \mathbf{p}_r, \mathbf{k}) \geq E_0, \\ \text{(ii) } \mathbf{p} \text{ is inside proton Fermi sphere,} \\ \text{(iii) } \mathbf{q} \text{ is outside neutron Fermi sphere} \end{cases} \\ &\equiv 0 \quad \text{elsewhere.} \end{aligned} \quad (\text{A6})$$

Therefore

$$\begin{aligned} J_{\text{rad}} &= \int \frac{d^3k}{k} d^3p_r \frac{\partial}{\partial E_0} \int d^3p \Theta(E_0, \psi) \\ &= \int \frac{d^3k}{k} d^3p_r \frac{\partial}{\partial E_0} V(E_0, \mathbf{p}_r, \mathbf{k}), \end{aligned} \quad (\text{A7})$$

²⁷ E_0 is equal to the rest energy of the muon diminished by the difference in rest energy of the final and initial nuclei in their ground states and by the K -shell binding energy of the muon in its lowest atomic state around the capturing nucleus.

where $V(E_0, \mathbf{p}, \mathbf{k})$ is the volume in \mathbf{p} space of the region for which $\Theta = 1$. It is not difficult to see from (A5) that the part of the bounding surface of the volume V which depends on E_0 is represented by the region on a plane (equation $\psi = E_0$) whose points \mathbf{p} lie inside the proton Fermi sphere and give rise to neutron momenta $\mathbf{q} = \mathbf{p} - (\mathbf{k} + \mathbf{p}_\nu)$ lying outside the neutron Fermi sphere.²⁸ The area of the allowed region on the plane $\psi = E_0$ is evidently a factor in the derivative $\partial V / \partial E_0$. This part of the discussion follows in detail the geometrical treatment given by Tiomno and Wheeler²⁹ in their consideration of ordinary muon capture using the Fermi gas model.

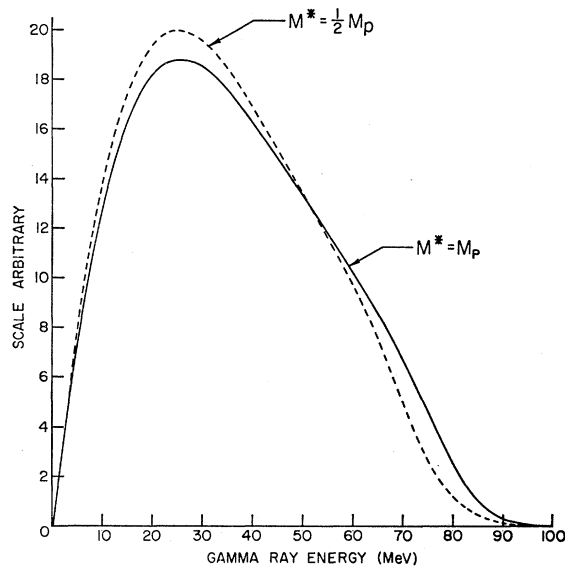


FIG. 14. Radiative capture gamma-ray spectra in copper for two values of effective mass.

²⁸ The neutron Fermi sphere is represented in the \mathbf{p} space as a sphere of radius q_0 with center displaced from the origin by the vector $\mathbf{k} + \mathbf{p}_\nu$.

²⁹ J. Tiomno and J. A. Wheeler, Rev. Mod. Phys. 21, 153 (1949).

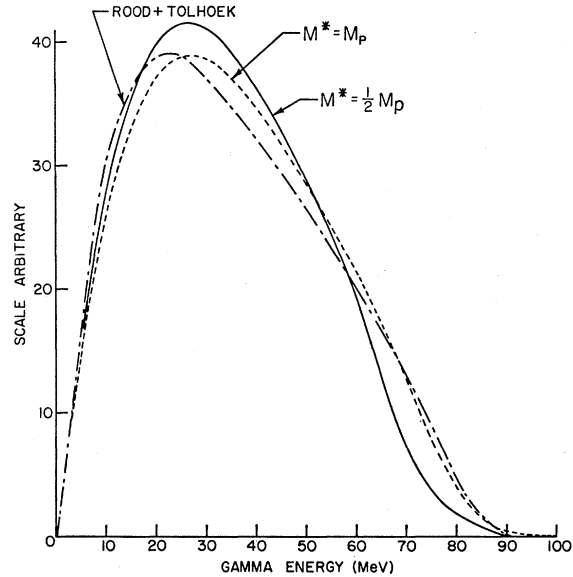


FIG. 15. Radiative capture gamma-ray spectra in calcium showing comparison with calculation by Rood and Tolhoek ($g_P/g_A = 8$).

Following evaluation of $\partial V / \partial E_0$, the final step is the integration over the direction and magnitude of \mathbf{p}_ν . Because of the complicated dependence on \mathbf{p}_ν of the intersections of the plane $\psi = E_0$ with the two Fermi spheres, the limits of integration on $\cos\theta_{\nu k}$ and on p_ν require careful handling. The integration over directions, $d\cos\theta_{\nu k}$, was carried out analytically, but it was more convenient to use numerical methods for the final integration on the magnitude, dp_ν .

Figure 14 shows the result. For the sake of comparison, a similar computation was performed for calcium-40 and compared to the spectrum obtained by Rood and Tolhoek.¹⁴ This is shown in Fig. 15 where the curves are normalized so as to have the same area. One can see that the spectra are quite similar especially for the case where $M^* = M_p$.